PERGAMON

International Journal of Multiphase Flow 25 (1999) 531–550

International Journal of Multiphase Flow

On a droplet's response to acoustic excitation

I.F. Murray, S.D. Heister

School of Aeronautics and Astronautics, Purdue University, W. Lafayette, IN, 47907, USA

Received 4 August 1996; received in revised form 18 August 1998

Abstract

The unsteady, nonlinear response of a liquid droplet to an imposed acoustic perturbation has been simulated using an algorithm based on boundary element methods (BEMs). The code was used to study the influence of the acoustic frequency, intensity, and gas/liquid density ratio upon the droplet behavior. Heightened droplet responses were observed for frequencies near the harmonics of the second and fourth mode frequencies. Several types of droplet atomization have been observed as the acoustic intensity is increased. Increasing gas density (at fixed excitation conditions) also heightens droplet response. © 1999 Elsevier Science Ltd. All rights reserved.

Keywords: Drop break up; Atomization; Drop dynamics; Acoustics; Drop oscillations

1. Introduction

The behavior of liquid droplets in the presence of an acoustic field is a phenomena of fundamental importance. There are a variety of applications in which droplets are excited by acoustic energy, such as meteorological physics, containerless processing, and atomization. Droplet oscillations in the absence of external excitation will ultimately dissipate, and the drop will return to its equilibrium state. However, a strong acoustic field may be present, such is the case in airborne combustors and acoustic levitators. In such a situation, the droplet will experience forced oscillations. This oscillatory behavior of drops may greatly affect the process of secondary atomization.

A large number of researchers have studied "free oscillations" of droplets under conditions where forces from the gaseous phase are neglected. The initial linear analyses of this problem are due to Rayleigh (1879) and Lamb (1982) for the inviscid and weak-viscous cases. These results provide the droplet's frequency of oscillation under various modes under the presumption that the shape perturbation is infinitessimal. Lamb's result indicates that weak

0301-9322/99/$ - see front matter
PII: S0301-9322(98)00051-2

viscous effects have a negligible effect on the frequency predicted by Rayleigh. Prosperetti (1980) furthered the linear analysis for arbitrary viscous effects.

More recently, theoretical/numerical efforts have focused on nonlinear effects. Tsamopoulos and Brown (1983) developed a theoretical series solution for moderate amplitude, inviscid droplet oscillations. They determined that the droplet resonant frequency decreases with the square of the oscillation amplitude. Lundgren and Mansour (1988) used a boundary integral method to investigate large amplitude oscillations of droplets in zero-gravity including weak viscous effects. They discovered that relatively small viscosities can significantly affect the coupling of oscillatory modes. However, their method was limited to only weak viscous problems. More recently, Basaran (1992) used the Galerkin/finite element technique to address nonlinear oscillations of viscous droplets. From these simulations he observed that a finite viscosity has a much larger effect on mode coupling than what is predicted by the calculations including weak viscous effects.

Experimental work in droplet oscillations has been conducted by Trinh and Wang (1982), in which large amplitude, nonlinear oscillations of drops were studied. In their studies, a neutrally-buoyant droplet was suspended in an immiscible liquid and excited by acoustic–radiation pressure forces generated by an acoustic levitator. More recently, Wang et al. (1996) studied the oscillations of low-viscosity drops in a microgravity environment on board the space shuttle using a similar acoustic chamber to induce droplet deformation. In these experiments, droplets were deformed and then allowed to oscillate freely. From a controlled break up of a liquid jet, Becker et al. (1991) generated virtually monodispersed droplets that oscillated in a damped, axisymmetric fashion. These experiments verified the reduction in natural frequency at finite amplitudes as predicted by Tsamopoulos and Brown.

Despite these advancements in the area of free-oscillation of droplets, there have been relatively few works aimed at increasing the understanding of droplet response to forced oscillations. Here, the experimental work of Daidzic (1995) is a notable exception. Using an acoustic levitator, Daidzic examined nonlinear forced oscillation of droplets. In his experiments the droplets exhibited "chaotic behavior", presumably because the forcing function was three-dimensional and time-dependent. He concluded that prediction of droplet behavior over a long period of time is difficult at best, and warrants further investigation.

The works of the aforementioned researchers have considerably improved the understanding of droplet behavior. However, the forced oscillation problem still warrants additional consideration. The focus of this work is to examine forced, nonlinear, inviscid droplet oscillations by computational analysis. The boundary element method (BEM) will be used to conduct these studies. This technique offers a savings in computational power as compared to other methods, such as computational fluid dynamics, while maintaining a high degree of accuracy. As the name implies, BEMs require the discretization of only the boundary of the domain, providing a drastic reduction in the total number of nodes (as compared to mesh based schemes) needed for an accurate solution. Hilbing, et al. (1995) and Mansour and Lundgren (1990) have also demonstrated a capability of running BEM simulations beyond atomization events. The following sections of this paper describe the development, validation, and results generated using this computational tool.

2. Model development

Under many situations, the wavelength of the acoustic perturbation is much greater than the droplet radius, which implies that spatial variations within the acoustic wave are negligible and that the disturbance can be modeled as an unsteady, incompressible flow. For example, a large liquid rocket engine will have acoustic wavelengths of the order of the chamber dimension (measured in cm), while droplet radii are typically measured in microns. Note that in many acoustic levitators this assumption may not be valid since the droplet diameter is a substantial fraction of the acoustic wavelength. In this case, spatial variations within the acoustic wave are important.

Further, we assume an axisymmetric domain and neglect viscosity in both gas and liquid phases. Under these conditions, the dynamics of both liquid and gas phases are described by Laplace's equation:

$$\nabla^2\phi = \nabla^2\phi_g = 0 \tag{1}$$

where ϕ and ϕ_g are velocity potentials for liquid and gaseous phases, respectively.

If we choose the droplet radius (a), peak speed in the acoustic disturbance (U), and liquid density (ρ) as dimensions, the interaction between the droplet and the acoustic disturbance is characterized by the gas/liquid density ratio,

$$\epsilon = \frac{\rho_g}{\rho} \tag{2}$$

the Weber number based on gas density,

$$We = \frac{\rho_g U^2 a}{\sigma} \tag{3}$$

and the frequency ratio,

$$\frac{\omega}{\omega_n}. \tag{4}$$

Changes in the magnitude of the acoustic disturbance are introduced through the Weber number, which is the ratio of the aerodynamic forces to surface tension (σ) forces. The frequency ratio is the ratio of the acoustic frequency of the gas, ω, to the linear natural frequency of the second mode for a liquid drop, ω_n. In the following development, we presume that the nondimensionalization described above has been applied.

The droplet's fundamental frequencies are obtained from the classic analysis by Lamb. The nondimensional form for the frequency of mode "m" is:

$$\omega_m^2 = \frac{m(m+1)(m-1)(m+2)}{(m+1+m\epsilon)We}. \tag{5}$$

For this case, the lowest-order ($m = 2$), or natural frequency of a droplet reduces to:

$$\omega_2^2 = \omega_n^2 = \frac{24}{(3+2\epsilon)We}. \tag{6}$$

We expect strong droplet response when the acoustic excitation frequency ω lies near harmonics of ω_n.

At any instant in time, Eq. (1) provides a connection between values of the velocity potentials and velocities measured normal to the local surface (q and q_g) for liquid and gaseous phases, respectively. This equation is solved using the BEM by beginning with its integral representation. For the liquid phase, the resulting integral representation of Eq. (1) becomes:

$$\alpha\phi(\vec{r}_i) + \int_T \left[\phi \frac{\partial G}{\partial \hat{n}} - qG\right] d\Gamma = 0 \tag{7}$$

where $\phi(\vec{r}_i)$ is the velocity potential at a point $\vec{r}_i$, Γ is the boundary of the domain, and G denotes the free space Green's function corresponding to Laplace's equation. In addition, $\hat{n}$ is taken to be the outward normal to the domain boundary, and α results from singularities introduced as the integration passes over the boundary point, $\vec{r}_i$. By using Eq. (7), it is possible to solve for ϕ or q provided that one of them is known at each point on the boundary. If we let r and z represent radial and axial coordinates and use the subscript i to denote the "base point" where the integration takes place, the free space Green's function for the axisymmetric Laplacian can be expressed (Liggett and Liu 1983):

$$G = \frac{4rK(p)}{\sqrt{(r+r_i)^2 + (z-z_i)^2}} \tag{8}$$

where

$$p = \frac{(r-r_i)^2 + (z-z_i)^2}{(r+r_i)^2 + (z-z_i)^2} \tag{9}$$

and, $K(p)$ is the complete elliptic integral of the first kind. For computational efficiency, this parameter is curvefit (to an accuracy of 10^{-8}) using results from Abramowitz and Stegun (1970).

The integration in Eq. (7) is performed by discretizing the boundary into a finite number of segments. Along each segment, both ϕ and q are assumed to vary linearly. Integrations are carried out by letting each node on the boundary represent a base point, yielding a set of linear equations relating ϕ and q involving all boundary nodes. The fully-populated matrices used to store coefficients of these equations are inverted using the Crout method LU decomposition from numerical recipes in Fortran (Press, et al. 1992). Additional details regarding the BEM solution procedure are provided in Hilbing et al. (1995).

2.1. Free surface treatment

A procedure similar to that of Longuet-Higgins and Cokelet (1976) is used to update the position of nodes on the interface. Free surface nodes are "tracked" along lines parallel to the local velocity vector *in the liquid*. Under this assumption, flow kinematics require:

$$\frac{Dr}{Dt} = \frac{\partial \phi}{\partial r} \quad \frac{Dz}{Dt} = \frac{\partial \phi}{\partial z}. \tag{10}$$

The velocities calculated by solving Laplace's equation are normal and tangential to the surface. While the normal velocity is generated via the solution of Laplace's equation, the tangential velocity ($\partial\phi/\partial s$) is calculated using a 4th-order (five point) centered difference method. Radial and axial velocities required in Eq. (10) are determined via the coordinate transformation:

$$\frac{\partial \phi}{\partial r} = \frac{\partial \phi}{\partial s}\sin\beta + q\cos\beta \tag{11}$$

and

$$\frac{\partial \phi}{\partial z} = \frac{\partial \phi}{\partial s}\cos\beta - q\sin\beta \tag{12}$$

where β is the local wave slope.

The unsteady Bernoulli equation provides the dynamic boundary condition for nodes on the interface. In an Eulerian system where time derivatives are assumed to occur at a fixed spatial location, the dimensionless form of this relation valid in the liquid domain is

$$\frac{\partial \phi}{\partial t} + \frac{1}{2}(\nabla\phi)^2 + P_g + \frac{\kappa}{We} = 0 \tag{13}$$

and the gas domain analog is

$$\epsilon\frac{\partial \phi_g}{\partial t} + \frac{\epsilon}{2}(\nabla\phi_g)^2 + P_g = 0. \tag{14}$$

Here, the surface curvature, κ, is computed using the parametric form due to Smirnov (1964) involving coordinate derivatives with respect to distance along the interface. All derivatives are computed using fourth-order centered differences in the numerical approximations to κ. Since the nodes on the interface are assumed to travel with the local liquid surface velocity, a transformation from the Eulerian to Lagrangian reference frame is required:

$$\frac{D(\,)}{Dt} = \frac{\partial(\,)}{\partial t} + \nabla\phi\cdot\nabla(\,). \tag{15}$$

By applying this transformation, the Bernoulli's Eqs. (13) and (14) become:

$$\frac{D\phi}{Dt} = \frac{1}{2}(\nabla\phi)^2 - P_g - \frac{\kappa}{We}, \tag{16}$$

$$P_g = -\frac{\epsilon}{2}(\nabla\phi_g)^2 - \epsilon\frac{D\phi_g}{Dt} + \epsilon\nabla\phi\cdot\nabla\phi_g \tag{17}$$

where $D()/Dt$ denotes changes in time for nodes moving with the liquid interface velocity.

In the case of the liquid domain, the substantial derivative, $D\phi/Dt$, is calculated using Eq. (16). A first order backward difference method was used to calculate the gas based substantial derivative appearing in Eq. (17):

$$\frac{D\phi_g}{Dt} = \frac{\phi_g^{n+1} - \phi_g^n}{\Delta t} \tag{18}$$

where n indicates the time level.

A stable, time-accurate procedure has been developed to advance the solutions of Eqs. (16), (17) for all free-surface nodes. The following steps are taken:

1. an initial value of ϕ and ϕ_g are given at each node on the interface;
2. solution of Laplace's equation (described in previous section) provides the liquid domain velocities, q, at each node on the interface;
3. set $q_g = -q$ since the gas nodes are fixed to move with the liquid nodes and the outward normals are in opposite directions;
4. solve Laplace's equations for the gas domain to calculate ϕ_g at each node in the gas;
5. calculate $D\phi_g/Dt$ using Eq. (8);
6. calculate the gas pressure distribution along the interface using Eq. (17);
7. this value of gas pressure is used to solve for ϕ at the new time step via integration of Eq. (16);
8. the interface is "regridded" using cubic splines of r, z, P_g, and ϕ to preserve the even spacing between nodes (Hilbing et al. 1995);
9. steps 2–4 are repeated with the "regridded" properties, in order to determine the boundary conditions at the next time step for the new grid.

A 4th-order Runge–Kutta scheme is employed in the time integrations for $D\phi/Dt$, Dr/Dt, and Dz/Dt. Using this scheme, it is necessary to solve the Laplace equation eight times, four for the liquid and four for the gas. However, at the end of each time step it is necessary to solve the Laplace equation for both domains again (due to the regridding), resulting in a total of ten Laplace solutions per time step using this procedure.

2.2. Domain discretization and boundary conditions

The time-dependent distortion of the droplet is driven by the instantaneous pressure distribution generated by the unsteady gas flow around the body. Since the outer flow is unsteady, a freestream pressure gradient is present across the drop. This pressure gradient leads to the virtual mass force which will cause translation of the droplet center of gravity with time. Prosperetti (1984) has shown that the velocity of droplet translation scales directly with the gas/liquid density ratio (ϵ) such that virtual mass effects are of vanishing importance when $\epsilon \ll 1$. In this case, we may simplify the domain required for axisymmetric computations by considering only the quadrant $r \geq 0$, $z \geq 0$, rather than the entire upper half plane. While we

will not be able to investigate virtual mass effects using this domain, it does provide a substantial reduction in the number of nodes (and hence run time) required for a given simulation. In addition, we have verified that the droplet distortion is not affected by this assumption; nearly identical distortion is obtained for a comparable model which utilized the entire upper half plane, thereby including virtual mass effects. Since the matrix inversions in the BEM approach scale as the cube of the number of nodes, the simplified domain provides a factor of eight in computational savings over the complete upper half-plane domain.

Under this assumption, the computational domain and the boundary conditions used in this analysis are displayed in Fig. 1. Gas nodes are denoted with an "x", while the liquid nodes are labeled with an "o". Along the radial line of symmetry for both domains, $q = 0$ in the liquid and $\phi_g = 0$ in the gas in order to support the assumption discussed above. We require the $\phi_g = 0$ condition to insure that no vertical velocities are present in the gas which provides a condition consistent with the neglect of droplet translation. Eqs. (16) and (17) were used to set the boundary condition along the interface. On the outer boundary of the gas domain, a sinusoidal velocity history is used to model the acoustic disturbance:

$$\phi_g = z_g \cos\left(\frac{\omega}{2}\right). \tag{19}$$

Here, the factor of 1/2 in the cosine argument is used to cause the harmonic condition to occur at $\omega = \omega_n$. Physically, the drop is distorted into a prolate shape by an acoustic wave traveling either to the left or to the right, so that the proper frequency to characterize the forcing function is actually $\omega/2$. Nodes are not required along the axis of symmetry (with the exception of the terminus of droplet and outer-gas boundaries) since the Green's functions vanish as $r \to 0$.

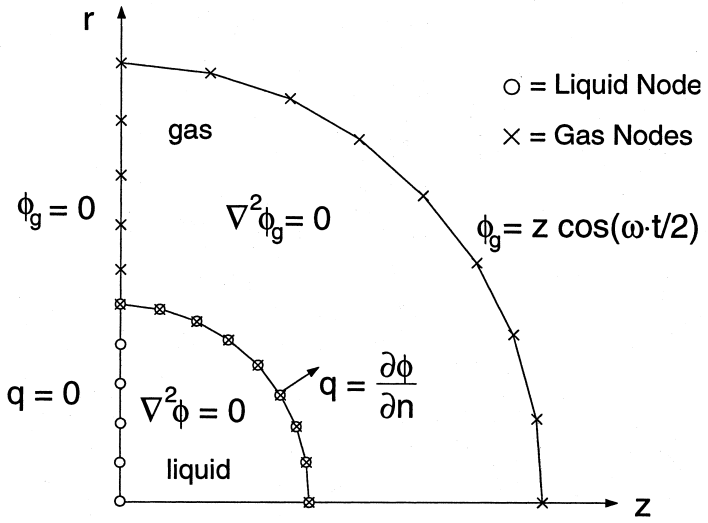

Fig. 1. Schematic of computational domain and boundary conditions.

3. Code implementation and validation

The accuracy of the algorithm was verified by comparing its results to various analytic and numerical solutions of related problems. Three separate validation cases were considered: steady flow over a sphere, non-linear oscillations of a liquid droplet, and droplet profiles for a steady crossflow.

The accuracy of the gas domain solution was tested by comparing the distribution of the velocity potential over a sphere with the analytic solution of the same problem. The analytic solution was compared to the numerical solutions for grids using, 45, 35, 25, and 15 nodes along the interface. The numerical results agree well with the analytic solution, and the magnitude of the error is well below 0.5% for all cases. For computational efficiency, it was decided to employ only 15 nodes to model the surface of the droplet. For cases when the drop becomes highly deformed, as many as 45 nodes were employed in order to adequately resolve the surface. Convergence studies indicate that the 45 node grid is adequate to represent all droplet shapes presented herein.

As explained previously, an expression for the fundamental oscillatory mode was developed by Lamb using linear analysis. This analysis assumed a linearized surface shape of the form:

$$r = 1 + \eta \cos(m\theta) \sin(\omega_n t) \tag{20}$$

where η is the measure of the initial disturbance amplitude. At finite deformations, the drop's natural frequency tends to be reduced when compared to Lamb's result. This effect has been

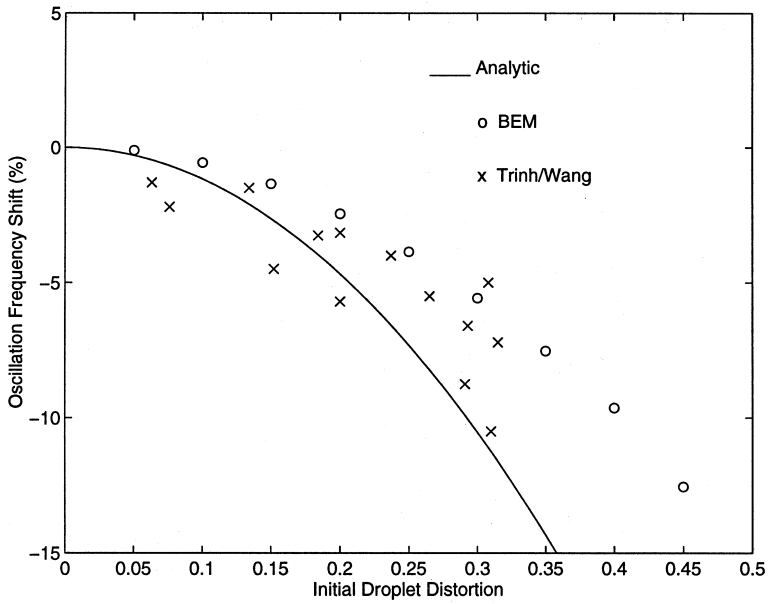

Fig. 2. Comparisons of predicted frequency shifts for nonlinear oscillations of a droplet.

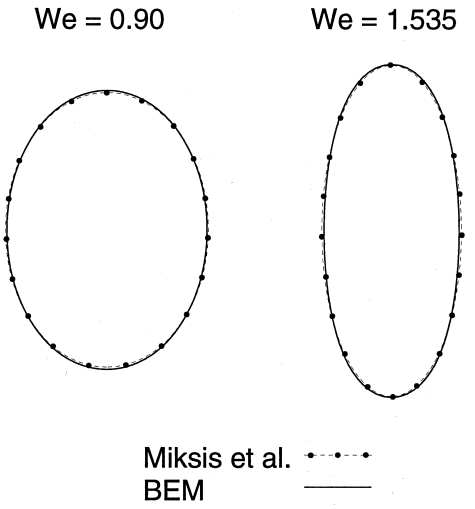

Fig. 3. Comparisons of steady state droplet profiles.

studied experimentally by Trinh and Wang (1982) and through the use of a second-order asymptotic analysis by Tsamopoulos (1988). The current calculations are compared with these results in Fig. 2 for various assumed levels of initial deformation of the drop. Here, the inviscid BEM solutions tend to predict the upper bound of the measurements of Trinh and Wang which utilized a neutrally-bouyant drop of silicon oil/carbon tetrachloride suspended in distilled water. While the current results agree reasonably well with the asymptotic predictions at low deformations, substantial differences are noted at higher deformation levels, presumably due to 4th-order effects not considered in the analytic treatment.

A final validation process involved verification of the accuracy of the model when there is a strong coupling effect between the gas and liquid domains. This was accomplished by comparing droplet profiles from the present calculations to those of Miksis, et al. (1981) who developed a model to predict the equilibrium shape of a droplet subjected to a uniform flow. The equilibrium drop profile was determined by balancing the pressure of the gas on the surface with the surface tension and internal pressure at the same point.

In order to achieve a steady state solution, it was necessary to introduce a dissipative mechanism, which ultimately yielded a steady state solution. Numerical smoothing was applied to ϕ until surface velocities vanished. Fig. 3 shows a comparison between the predicted profiles of the numerical model and the method used by Miksis et al. showing excellent agreement between the two simulations.

4. Results

The algorithm was utilized to assess the influence of perturbation frequency (ω/ω_n), Weber number (We), and density ratio (ϵ) on the nonlinear response of a droplet to an imposed

acoustic oscillation. The results presented here represent over 200 runs of the code. Calculations typically used 15 nodes along the interface, 15 along the radial axis in the gas, and 10 nodes along the outer boundary of the gas domain. However, larger grids (as many as 45 nodes along the interface) were utilized to resolve more complex droplet shapes, such as those in Fig. 14 described below.

During these simulations, the level of the droplet response is characterized by two parameters, the aspect ratio and the oscillatory mode coefficients. The aspect ratio provides a gross measure of overall droplet deformation and is defined as being the ratio of the major axis over the minor axis of the droplet at peak deformation. The mode coefficients, are determined by expressing the current droplet shape as a sum of Legendre polynomials:

$$r = 1 + \sum_{m=1}^{\infty} C_m(t)\cos(m\theta) \tag{21}$$

where θ is the angle measured from the positive z axis and C_n are the time varying coefficients. Because cosine functions are orthogonal, it is possible to calculate the coefficients using (Lundgren and Mansour 1988):

$$C_m = \frac{1}{\pi}\int_{-\pi}^{\pi} (r-1)\cos(m\theta)\,\mathrm{d}\theta. \tag{22}$$

Due to the fact that both incompressible and inviscid assumptions are employed in the gas phase, there is no mechanism to generate a surface pressure distribution which is asymmetric about the r axis in Fig. 1. For this reason, the model cannot excite odd modes of oscillation. This fact was verified by demonstrating that mode coefficients for the odd modes were all zero to within machine accuracy (10^{-14}).

4.1. Frequency response spectrum

The effect of the acoustic perturbation frequency was investigated by performing approximately 100 simulations. While the frequency was varied, the Weber number was held at 0.5779 and the density ratio was 0.00123. These conditions correspond to acoustic excitation of a 100 micron water droplet with a 160 db disturbance in ambient air. Droplet translational velocities due to virtual mass effects, which are neglected as described previously, will be of the order of 0.1% of the peak acoustic velocity for this density ratio. A time step of 0.05 was employed for these computations. Results are displayed on Fig. 4, which charts the aspect ratio for a range of frequency ratios. Readers are cautioned that the purpose of this investigation is to determine regions of high response; actual aspect ratios do depend on the assumed initial conditions (spherical vs deformed drop, sine wave vs cosine wave disturbance).

Fig. 4 displays a series of peaks that occur near the harmonics of the natural frequency of the droplet. A noteworthy area is the break up region that exists for frequency ratios between 0.80 and 0.90. In this band, the disturbance is tuned to the natural frequency of the droplet to an extent such that atomization occurs. All peaks are shifted to frequencies slightly less than the linear result due to the nonlinear frequency shift as shown in Fig. 2. The continual shifting of droplet natural frequency with deformation level leads to a bounded response over much of the frequency range (for this Weber number). In these regions, the acoustic perturbation

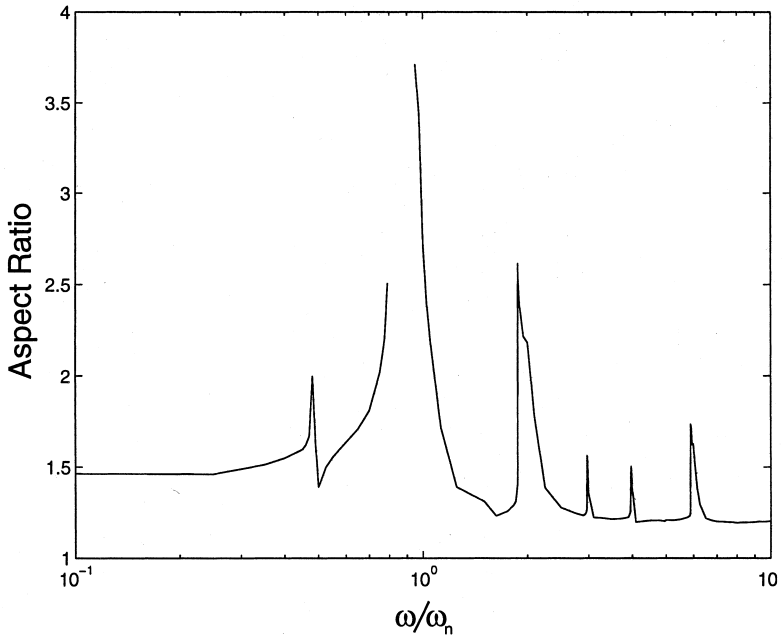

Fig. 4. Frequency response spectrum.

continues to excite the droplet until the oscillations of the drop become out of phase with the disturbance, thereby tending to reduce the amplitude of the oscillation. This process repeats indefinitely or until the drop breaks up.

Areas of significant response occur for ω/ω_n = near 0.5, 1.0, 2.0, 3.0, 4.0, and 6.0. The peaks near $\omega/\omega_n = 0.5$, 1.0, and 2.0 are primarily driven by second mode oscillations, while the peaks near $\omega/\omega_n = 3.0$, 4.0, and 6.0 contain significant fourth-mode effects. It is important to note that the fundamental frequency of the fourth mode is three times that of the fundamental frequency of the second mode, $\omega_4 = 3\ \omega_n$, for a drop in a low density gas ($\epsilon \ll 1$). It is worth mentioning that a frequency ratio near 5.0 does not produce a notable response.

For relatively low disturbance frequencies ($\omega \gg \omega_n$), a quasi steady-state response is observed whereby the droplet closely tracks the imposed perturbation with a very small phase lag. The amplitude (aspect ratio) in this region is greater than the response for higher off-harmonic frequency ratios due to the negligible phase lag in this region. At the other extreme ($\omega \gg \omega_n$) the oscillations of the gas are so fast that the droplet is unable to respond appreciably to the changes in the gas flow. Here, the droplet responds to a mean dynamic pressure generated by the acoustic wave.

As the frequency ratio approaches a value of 0.5, the droplet begins to experience a sub-harmonic excitation. The frequency of its oscillation is 0.0604, which is approximately half of the natural frequency, 0.1304. The droplet behavior is characterized by a large deformation followed by a smaller one. The larger response is attributed to the peaks in the acoustic wave, whereas the secondary response is due to the droplet attempting to maintain its natural frequency. It has been observed that the second mode is solely responsible for the activity.

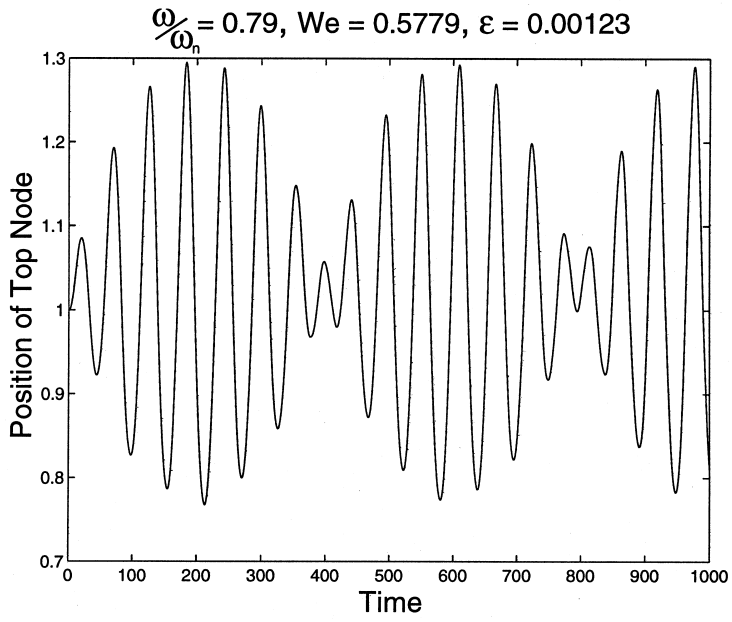

Fig. 5. Time history of top node position.

There is a negligible amount of fourth mode activity, and the higher order modes are virtually non-existent (Murray, 1996).

For frequency ratios near the drop natural frequency, the level of droplet activity is high, such is the case for $\omega/\omega_n = 0.79$. Fig. 5 displays the radial position of the node at $z = 0$ on the interface for this frequency ratio. As the droplet begins to deform, the reduction in its natural frequency drives it toward a harmonic condition with the imposed disturbance. At very large deformation, the droplet natural frequency drops to the the point where the acoustic wave provides destructive interference, i.e. the forcing signal is out of phase with the droplet oscillation. A reduction in droplet response occurs in this time frame. Eventually, the droplet deformation is small enough so as to place its natural frequency near that of the acoustic wave and growth in amplitude is observed again. The overall period of this envelope of oscillations is $T = 398$, which represents (approximately 6 1/2 oscillations of the imposed gas disturbance). The droplet shapes at various times in this process are summarized in Fig. 6.

The activity of the droplet is initially controlled by second mode effects. The time history of the mode coefficients for the $\omega/\omega_n = 0.79$ case is shown in Fig. 7. As the oscillatory amplitude increases, fourth mode coupling appears. As in all results investigated in this study, 6th, 8th, and higher even modes gave negligible contributions to the instantaneous droplet shapes. In conjunction with the nonlinear frequency shift, the fourth mode effects have a stabilizing influence upon the droplet. Fig. 8 indicates that the second and fourth modes become coupled and destructively interfere, which causes the magnitude of the oscillations to dampen and the fourth mode effects to vanish. A similar envelope response is observed for the $\omega/\omega_n = 0.925$ case, however, the interference that occurs is somewhat constructive, which serves to amplify the response.

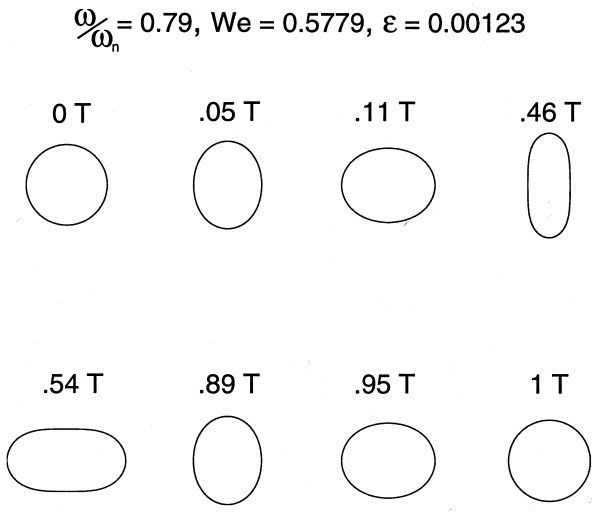

Fig. 6. Time history of droplet profiles.

For frequency ratios between 0.79 and 0.925, the second mode effects become overwhelming and the droplet breaks up. As the frequency ratio increases past 0.925, the droplet activity drops off since the excitation is above the resonant condition for finite deformation of the drop. A region of moderate droplet response lies in the frequency range of 1.2 to 1.4, which corresponds to the subharmonic of the fourth mode. Significant response is also noted at the second-harmonic of the fundamental mode, as one would expect.

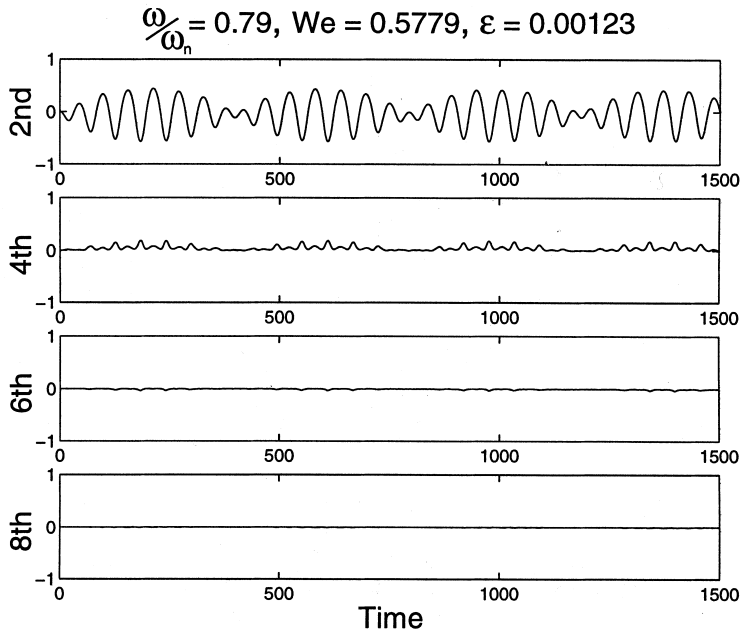

Fig. 7. Time history of mode coefficients.

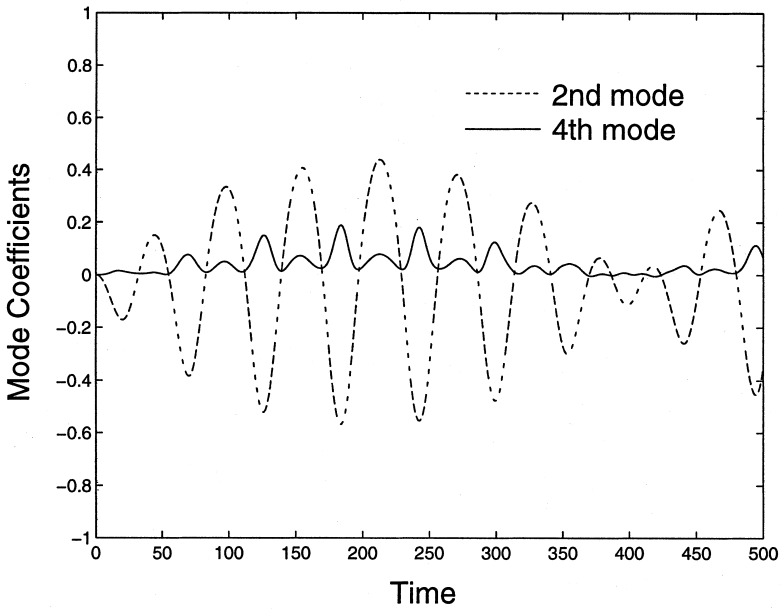

Fig. 8. Oscillatory mode interference.

For a frequency ratio near 3.0, the droplet experiences the third harmonic of the second mode of oscillation as well as the fundamental frequency of the fourth mode of oscillation. The time histories of the position of the node at $z = 0$ and the mode coefficients are presented in

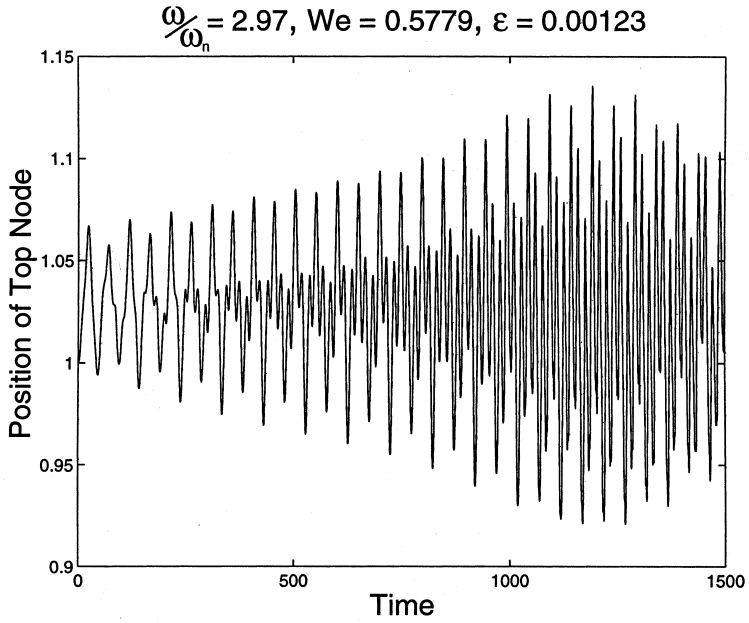

Fig. 9. Time history of top node position.

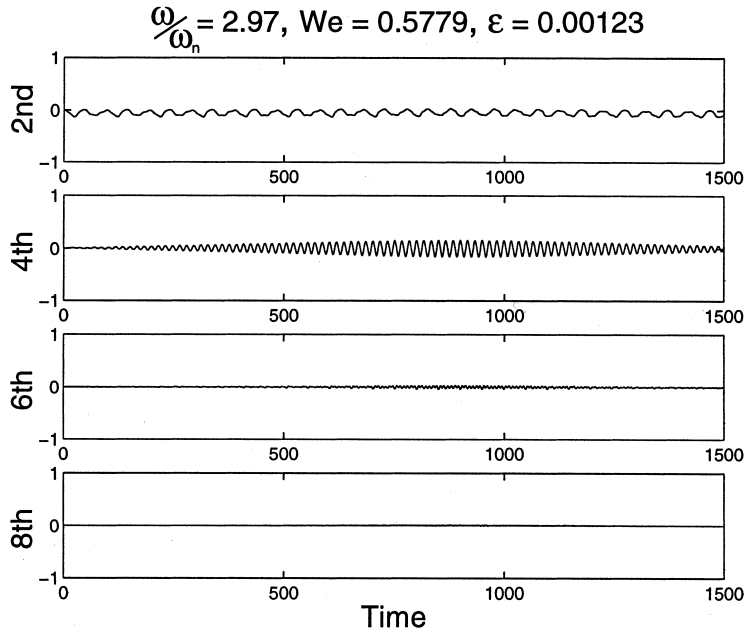

Fig. 10. Time history of mode coefficients.

Fig. 9 and 10. The overall period for the process is over 2500, during which over 150 gas oscillations occur. Throughout this process, the magnitude of the second mode remains reasonably constant, whereas the fourth mode grows and decays over the period. Initially, the

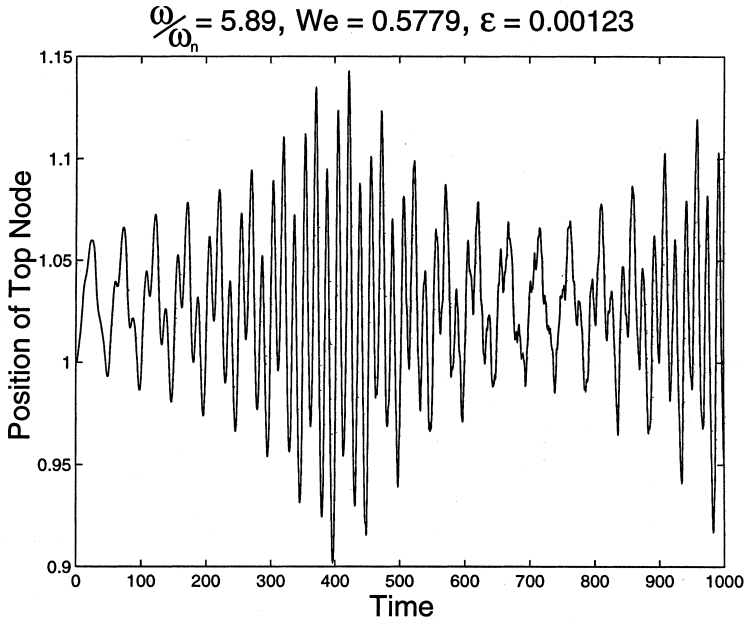

Fig. 11. Time history of top node position.

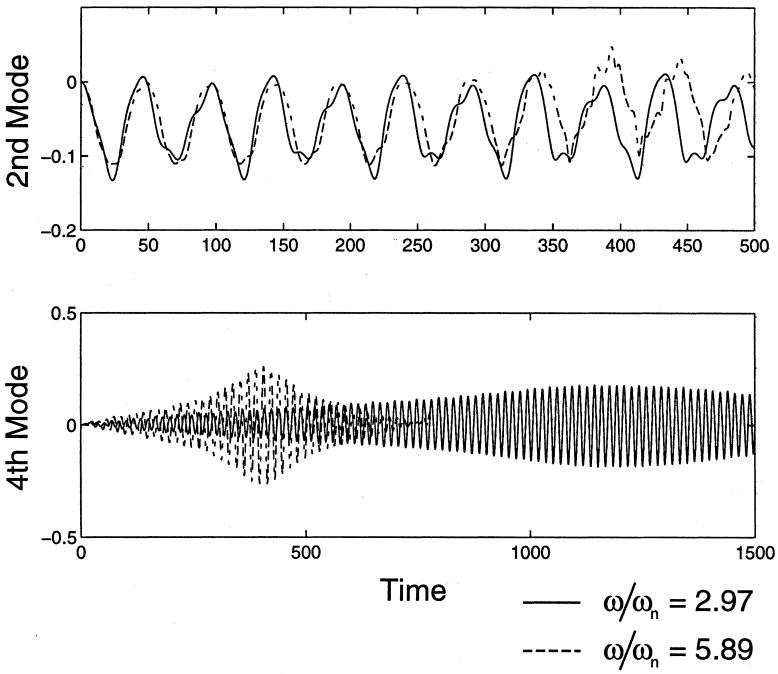

Fig. 12. Second and fourth mode coefficients.

droplet oscillates in the second mode. As the fourth mode grows, it dominates the behavior of the droplet. The fourth mode then decays to roughly the same order of magnitude as the second mode. Similar behavior is observed for $\omega/\omega_n = 3.975$.

Probably the most surprising result from the frequency spectrum is that *more* response is noted near the second harmonic of the fourth mode ($\omega/\omega_n \approx 6$) than at the primary fourth mode excitation frequency. These two peaks were the subject of substantial scrutiny; results were replicated for several different timesteps and mesh sizes. The position history for the node at $z = 0$ for this case is shown in Fig. 11. Here, the overall process takes about 780 dimensionless s, corresponding to about 95 periods of acoustic excitation. To seek an explanation for the heightened response (as compared to the $\omega/\omega_n = 2.97$ case), the second and fourth mode coefficients are compared in Fig. 12. As seen in the upper plot, the second mode response is similar in both cases. However, the lower plot reveals a heightened fourth mode response near $t = 400$ for the $\omega/\omega_n = 5.89$ case. Apparently, there is a constructive nonlinear interaction in the $\omega/\omega_n = 5.89$ case leading to stronger fourth mode effects and increased overall excitation. Since viscous effects are more prevalent in damping higher modes, this curious response may not be replicated in actual experiments.

4.2. *Effect of acoustic disturbance intensity*

The influence of the intensity of the acoustic wave was investigated by conducting a series of simulations at fixed density and frequency ratios, but with varying Weber number. For these simulations, the time step was set to be approximately 1/1000 of the period of a droplet

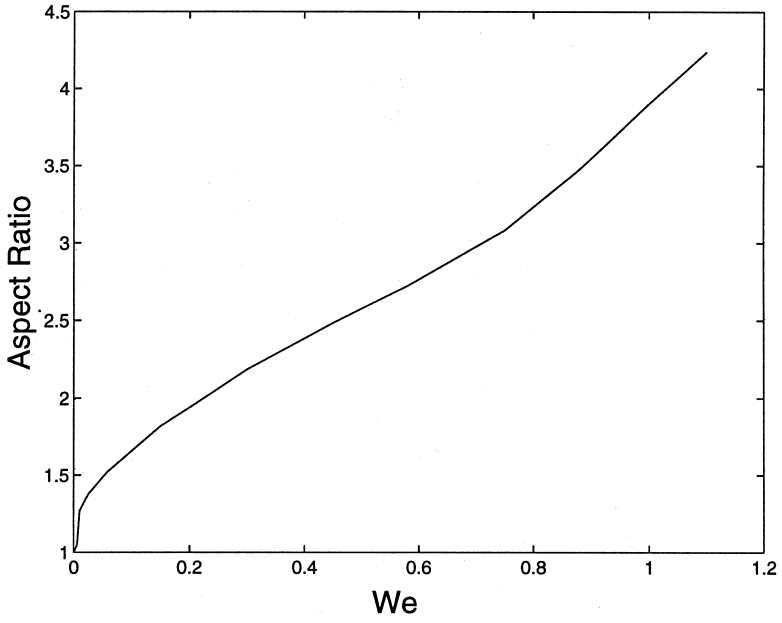

Fig. 13. Effects of the Weber number upon droplet behavior ($\epsilon = 0.00123$, $\omega = \omega_n$).

oscillation for the $m = 2$ mode. Once again, the aspect ratio was used as an overall measure of droplet response; Fig. 13 provides results for the case $\epsilon = 0.00123$, $\omega/\omega_n = 1.0$. During these simulations, it was observed that droplet atomization occurred at Weber numbers above 1.10. Here it is important to note that this "critical Weber number" is dependent on both density and frequency ratios; the 1.10 value is for harmonic excitation of a water droplet in air ($\epsilon = 0.00123$).

Droplet break up was studied by conducting trials using Weber numbers greater than the critical value. From this analysis, three regimes of break up were identified. Examples of these modes are shown in Fig. 14. In the "nipple" breakup regime ($1.1 < We < 2.5$), two small satellite droplets are formed as a result of the nonlinear motion of the drop. Since the acoustic intensity is barely above the threshold value, breakup in this region takes a substantial amount of time. The nipple regime is similar to the mode of break up experienced in the break up band of frequencies, as discussed in the beginning of Section 4.1. As the Weber number is increased to 2.5, atomization occurs with the formation of two satellite droplets which are larger than the central drop. The "kidney" regime exists for $2.5 < We < 3.0$ and is characterized by breakups which occur in 1–2 periods of the acoustic wave.

At large Weber numbers, the drop flattens out in the direction perpendicular to the gas flow, and the center continues to flatten which results in the pushing out of a toroid of fluid. Break up occurs when the center of the drop pinches, and the cross-section resembles a torus. Atomization in this "toroidal" mode occurs in less than one acoustic period for $We \geq 3.0$. Here, the droplet rapidly flattens in a plane perpendicular to the acoustic wave. With increasing Weber number, the overall diameter of the droplet (at the atomization point) increases, while the inner diameter of the torus decreases as shown in Fig. 14. In this figure, the $We = 5.78$ case is at a reduced scale for display purposes. The droplet shapes at high We

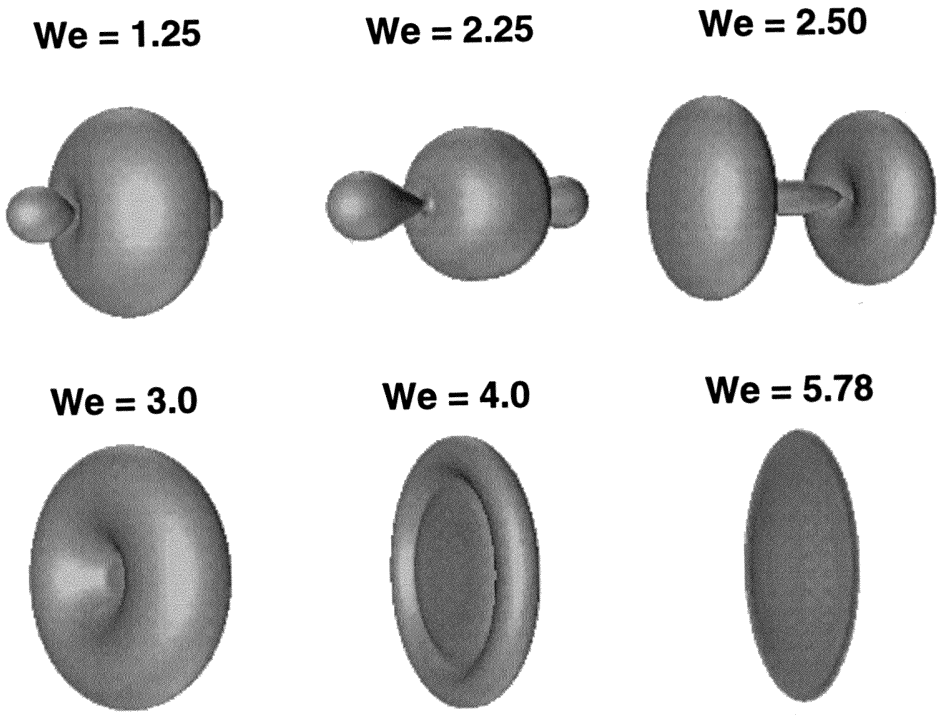

Fig. 14. Weber number induced droplet break up profiles ($\epsilon = 0.00123$, $\omega = \omega_n$).

values are consistent with "aerodynamic shattering" which has been documented by observing the response of a droplet to a shock wave (see Hsiang and Faeth (1992) for background).

A summary of the breakup times are provided in Fig. 15. Here, times are measured from the initiation of the acoustic forcing and are nondimensionalized by the period of the acoustic waveform. The curve is somewhat discontinuous in places due to the fact that breakups occur within discrete parts of a given cycle. Once again, for the conditions noted, no breakups occurred for $We < 1.1$.

5. Conclusions

The algorithm presented in this paper has been used to study the nonlinear evolution of an acoustically excited droplet. While the maximum response of the droplet occurs at the harmonic condition ($\omega = \omega_n$), significant responses also occur for ω/ω_n near values of 0.5, 2, 3, 4, and 6. The actual peak responses are also slightly less than these values as a result of the reduction in the droplet's natural frequency at finite deformation amplitude (nonlinear frequency shift). Droplet responses for the frequency ratios near 0.5 and 2.0 are dominated by the second mode, whereas the coupling of the second and fourth modes are responsible for the responses to the frequency ratios near 3.0 and 4.0. The droplet response for $\omega/\omega_n \approx 6$, which

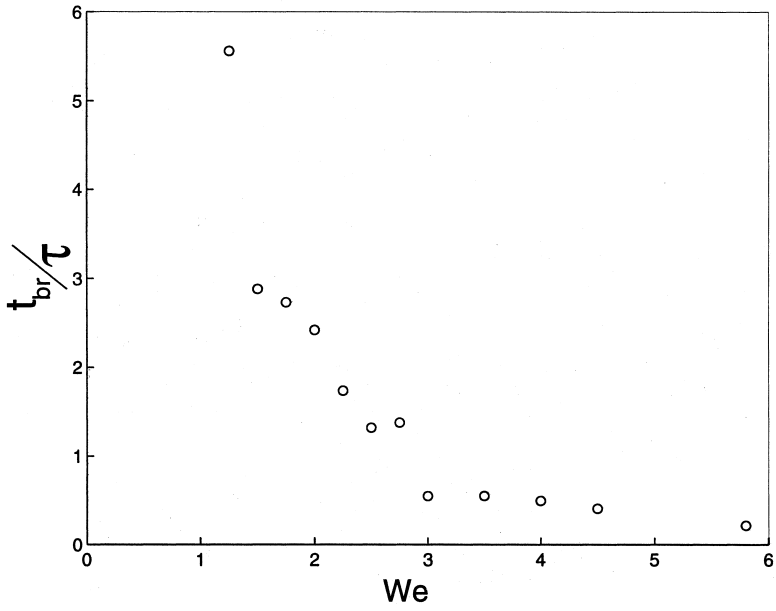

Fig. 15. Time required for droplet break up for various Weber numbers ($\epsilon = 0.00123$, $\omega = \omega_n$).

represents the second harmonic of the fourth mode, is dominated by fourth mode activity and the amplitude of the response actually exceeds that of some of the lower-order harmonics.

As the magnitude of the acoustic disturbance increases, droplet atomization is predicted to occur. For harmonic forcing of a liquid droplet in air, a critical Weber number of 1.10 divides the oscillatory and atomization regimes. Droplet breakups occurred in "nipple", "kidney", and "toroidal" modes as the Weber number was increased above this threshold value. Break up times were roughly inversely proportional to the Weber number under these conditions. Finally, increasing gas/liquid density ratio under fixed a Weber number and frequency ratio conditions was also shown to heighten droplet response.

Acknowledgements

The authors gratefully acknowledge the support of this work by the Air Force Office of Scientific Research under contract number F49620-93-1-0363 monitored by Dr Mitat Birkan. The authors also wish to acknowledge useful discussions with Professor Marc Williams of Purdue University.

References

Abramowitz M, Stegun FA, (Eds) 1970. Handbook of Mathematical Functions. 9th ed. Dover, New York.
Basaran, O., 1992. Nonlinear oscillations of viscous liquid drops]. Journal of Fluid Mechanics 241, 169–198.

Becker, E., Hiller, W., Kowalewski, T., 1991. Experimental and theoretical investigation of large amplitude oscillations of liquid droplets. Journal of Fluid Mechanics 231, 189–210.

Daidzic, N., 1995. Nonlinear droplet oscillations and evaporation in an ultrasonic levitator. Ph.D dissertation, Technical University of Erlangen–Nurnberg.

Hilbing, J.H., Heister, S.D., Spangler, C.A., 1995. A boundary element method for atomization of a finite liquid jet. Atomization and Sprays 5, 621–638.

Hsiang, L-P., Faeth, G.M., 1992. Near-limit drop deformation and secondary breakup. Int. J. Multiphase Flow 18, 635–652.

Lamb, H., 1982. Hydrodynamics. 6th ed.. Dover, New York.

Liggett, J.A., Liu, P.L-F., 1983. The Boundary Integral Equation Method for Porous Media Flow. George Allen and Unwin, London.

Longuet-Higgins, M.S., Cokelet, E.D., 1976. The deformation of steep surface waves on water, I, a numerical method of computation. Proceedings of the Royal Society of London A 350, 1–26.

Lundgren, S., Mansour, N.N., 1988. Oscillations of drops in zero gravity with weak viscous effects. Journal of Fluid Mechanics 194, 479–510.

Mansour, N.N., Lundgren, T.S., 1990. Satellite formation in capillary jet breakup. Physics of Fluids 2, 1141–1144.

Miksis, M., Vanden-Broeck, J., Keller, J., 1981. Axisymmetric bubble or drop in a uniform flow. Journal of Fluid Mechanics 108, 89–100.

Murray, I.F., 1996. Modeling acoustically-induced oscillations of droplets. MS thesis. Purdue University.

Press, W.H., Teukolsky, S.A., Vetterling, W.T., Flannery, B.P., 1992. Numerical Recipes in FORTRAN, The Art of Scientific Computing. Cambridge University Press, New York.

Prosperetti, A., 1980. Free oscillations of drops and bubbles: the initial value problem. Journal of Fluid Mechanics 100, 333–347.

Prosperetti, A., 1984. Acoustic cavitation series: part three, bubble phenomena in sound fields: part two. Ultrasonics 22, 115–124.

Rayleigh, L., 1879. On the capillary phenomenon of jets. Proceedings of the Royal Society of London 29, 71–97.

Smirnov, V.I., 1964. A Course of Higher Mathematics, vol. II. Pergamon Press, New York.

Trinh, E., Wang, T., 1982. Large-amplitude free and driven drop shape oscillations: experimental observations. Journal of Fluid Mechanics 122, 315–338.

Tsamopoulos, J.A., 1988. Nonlinear dynamics and breakup of charged drops. AIP Conference Proceedings 197, 3rd International Colloquim for Drops and Bubbles, pp. 169–187.

Tsamopoulos, J.A., Brown, R.A., 1983. Nonlinear oscillations of inviscid drops and bubbles. Journal of Fluid Mechanics 127, 519–537.

Wang, T., Anilkumar, A., Lee, C., 1996. Oscillations of liquid drops: results from USML-1 experiments in space. Journal of Fluid Mechanics 308, 1–14.